nanomaterials

MDPI

Article

TCAD Simulation of Resistive Switching Devices: Impact of ReRAM Configuration on Neuromorphic Computing

Seonggyeom Kim and Jonghwan Lee *

Department of System Semiconductor Engineering, Sangmyung University, Cheonan 31066, Republic of Korea
* Correspondence: jhlee77@smu.ac.kr

Abstract: This paper presents a method for modeling ReRAM in TCAD and validating its accuracy for neuromorphic systems. The data obtained from TCAD are used to analyze the accuracy of the neuromorphic system. The switching behaviors of ReRAM are implemented using the kinetic Monte Carlo (KMC) approach. Realistic ReRAM characteristics are obtained through the use of the trap-assisted tunneling (TAT) model and thermal equations. HfO_2-Al_2O_3-based ReRAM offers improved switching behaviors compared to HfO_2-based ReRAM. The variation in conductance depends on the structure of the ReRAM. The conductance extracted from TCAD is validated in the neuromorphic system using the MNIST (Modified National Institute of Standards and Technology) dataset.

Keywords: neuromorphic computing; memristor; TCAD (technology computer-aided design); ReRAM (resistive random-access memory); KMC (kinetic Monte Carlo)

check for updates

Citation: Kim, S.; Lee, J. TCAD Simulation of Resistive Switching Devices: Impact of ReRAM Configuration on Neuromorphic Computing. *Nanomaterials* **2024**, *14*, 1864. https://doi.org/10.3390/nano14231864

Academic Editor: Chunchang Wang

Received: 25 October 2024
Revised: 15 November 2024
Accepted: 20 November 2024
Published: 21 November 2024

1. Introduction

Numerous new technologies such as big data, cloud computing, machine learning, and artificial intelligence are being developed and used. With technological advancements, the volume and complexity of data increases. A wide variety of intelligent applications are now mostly based on neural networks [1,2]. Neural network-based systems require large amounts of data and heavy computation for learning and deriving inferences. Therefore, it is necessary to develop memory devices based on new operating principles, innovative structures, and new materials [3]. Recently, there has been a focus on research into energy- and space-efficient devices. These include ultra-flexible origami tessellations with shape memory properties that can be integrated with electronic devices, and organic electrolyte transistors that can perform sensing, memory, and processing functions [4,5]. Traditional von Neumann computing-based systems are powerful for logical computations, but not efficient for neural network computations [6,7]. This is because the implementation of efficient neural networks requires both parallel synapse storage and computation [8]. The neuromorphic computing system (NCS) has been proposed as a solution to enhance the efficiency of neural network implementation. The NCS is a system that mimics the human brain. It is characterized by low power consumption and high-efficiency processing. Moreover, it enables the coexistence of data processing and storage. Research on NCSs is exploring two-terminal systems using memristors and crossbar structures, and three-terminal systems using ion-gated vertical transistors (IGVTs), carbon-based nanomaterials such as carbon nanotubes (CNTs) and graphene, and polymers [9–11]. NCSs use a memristor device as the synaptic unit and a crossbar structure for parallel computation [12]. Memristors are known to be suitable for neuromorphic systems due to their high-speed operation and low power consumption [13].

The memristor is a compound word for a memory device and a resistor, meaning a device that can serve as a memory device and a resistor [14]. Furthermore, it is categorized by material, including resistive random-access memory (ReRAM), phase-change random-access memory (PCRAM), and ferroelectric random-access memory (FeRAM).

ReRAM is a memory that utilizes changes in resistance, storing "1" for low resistance and "0" for high resistance. The strengths of ReRAM include low operating voltage, low power consumption, high speed, and high density [15]. However, there are unresolved issues regarding materials, stability, and storage mechanisms [16]. PCRAM is a nonvolatile memory technology that exploits phase changes in materials for memory. Depending on the crystalline state of a material, it can switch between a crystalline state ("1" state) and an amorphous state ("0" state). The crystalline state is characterized by high optical reflectivity and low resistivity, while the amorphous state exhibits low optical reflectivity and high resistivity. PCRAM has the advantages of rapid read access, high density, and nonvolatility [17]. Meanwhile, it has the disadvantages of slower switching speed and higher power consumption than other memristor devices [18]. FeRAM displays nonvolatile resistive switching when the ferroelectric polarization direction of films reverses [19]. FeRAM offers nonvolatility, low power consumption, and fast operation, but faces challenges such as manufacturing difficulty, limited data retention time, and small memory capacity [20].

ReRAM is considered a promising device for modeling the features of biological synapses [21,22]. Although ReRAM has advantages in cell size and multi-bit capability, it has a higher energy consumption per bit than organic transistor, but smaller compared to conventional devices [23]. Furthermore, the ReRAM manufacturing process is similar to complementary metal-oxide semiconductors (CMOSs), so it does not incur any additional costs [24]. In particular, filament-based ReRAM provides low-power operation and excellent scalability [25]. In this study, the Synopsys's Sentaurus technology computer-aided design (TCAD) is used to develop HfO_2-based multilayer-structured ReRAM and identify its characteristics. The conductance is an important factor that affects accuracy in neuromorphic computing [15,24], and different types of conductance are verified depending on structures and input pulses. The accuracy is verified with NeuroSim using the MINST (Modified National Institute of Standards and Technology) data [26].

2. ReRAM Features

2.1. ReRAM Device Physics

Typically, the structure of ReRAM has metal–insulator–metal (MIM), where an insulator is sandwiched between metal electrodes. Oxide-based ReRAM devices operate based on redox reactions [24]. In ReRAM devices, redox reactions result in the formation of filaments (bridges) in the insulating layer between two metal electrodes. Memory storage has "0" and "1" states. A value of 0 means no data are stored, and a value of 1 means data are stored. The formation/rupture of the filaments induces the connection and disconnection of conductive paths between the two metal layers. This leads to the transition between low-resistance and high-resistance states [27,28]. A switch from HRS to LRS is called the SET process, and that from LRS to HRS is called the RESET process.

In most cases, a formation voltage greater than the SET voltage is required to induce a resistive switching operation in the initial device, and this operation is known as the forming process [29,30]. Figure 1 shows the operation of the RESET and SET processes. The switch between HRS and LRS is explained by the formation and rupture of conductive filaments within the insulator. These filaments comprise oxygen vacancies (V_o) or metal deposits. It is proposed that the movement of oxygen ions/vacancies stimulated by Joule heating and electric fields is critical for switching [31].

2.2. ReRAM Materials

Materials used in ReRAM devices include Pt, Au, and TiN for electrochemically inert electrodes, Ti, Ni, Ta, Al, and Cu for active metal electrodes, and CuO_x, TaO_x, AlO_x, SiO_x, ZrO_x, TiO_x, and HfO_x for insulating layers [32,33]. Oxide-based ReRAM operates based on the movement of anions, wherein oxygen vacancies form a conductance pathway within the insulating layer. Typically, an electrode that absorbs oxygen is required to facilitate anion movements [34]. HfO_2 has been widely used as ReRAM materials due to its excellent CMOS compatibility. In HfO_2-based ReRAM devices, TiN is commonly used as the electrode.

TiN is utilized as an oxygen scavenger to remove oxygen ions from the HfO_2 layer and functions as an oxygen reservoir. Most conductive filaments in HfO_2 are composed of oxygen vacancies and are commonly used due to their high dielectric constant and excellent thermal and chemical stabilities. The switching characteristics of ReRAMs are more stable when combined with active metal electrodes, compared to HfO_2 monostructures, due to the oxygen adsorption effect [35,36]. It is also reported that using a multilayer structure improves reliable switching and durability compared with employing a single insulating layer [37–39].

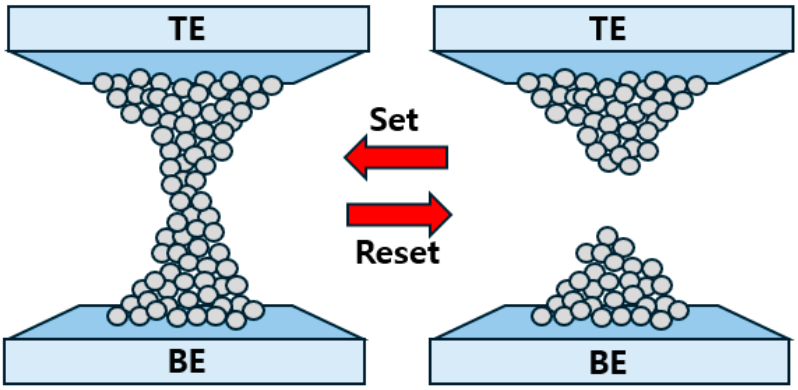

Figure 1. Operating principle of ReRAM. Set and Reset represent the formation and rupture of the filament, respectively.

3. TCAD Modeling

The simulation utilizes the Sentaurus TCAD of Synopsys. TCAD is a tool used for developing and optimizing semiconductor processing technologies and devices via computer simulations. TCAD is widely used in the semiconductor industry. Despite its complex process technology, the use of TCAD reduces development costs and accelerates research. The widely recognized physical schematic of ReRAM switching is shown in Figure 2 [40].

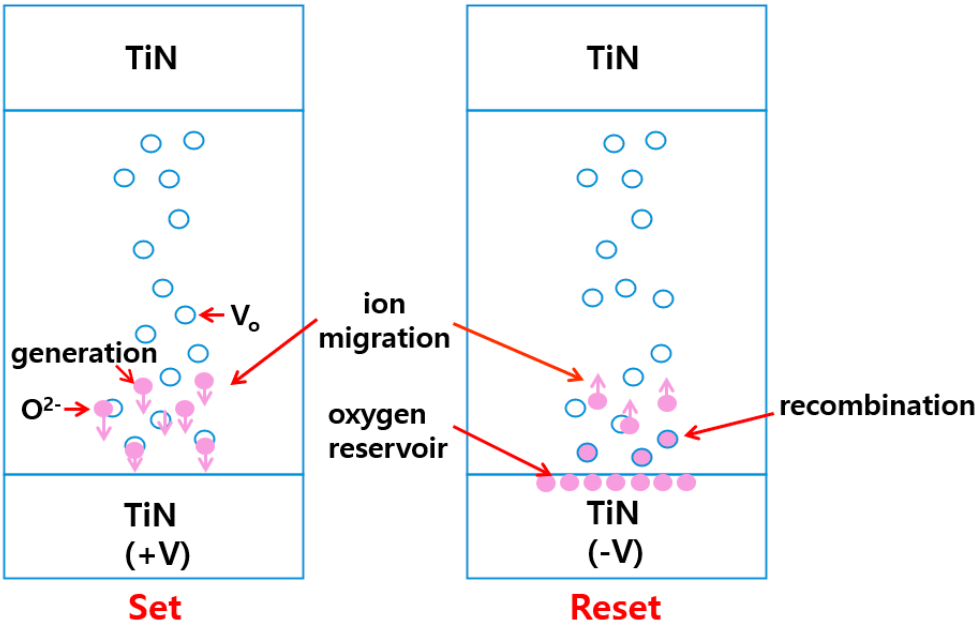

Figure 2. Schematic of the SET–RESET mechanism of metal oxide-based ReRAM.

The switching properties are related to the geometry of filaments owing to the direct result of the generation and recombination of oxygen vacancies within the insulating

layer [40,41]. In the SET process, oxygen ions are removed from the lattice and migrate to the active electrode, leaving behind a conductive filament formed from oxygen vacancies, which reduces resistance. During the RESET process, a negative (−) voltage is applied, causing oxygen ions stored at the electrode–dielectric junction to migrate to the insulating layer, where they recombine with oxygen vacancies and break the filament, increasing resistance [31,41]. To describe the switching of oxide-based ReRAM, the behaviors of electrons and ions must be considered, and their random nature must be reflected upon. To reflect their random nature, the kinetic Monte Carlo (KMC) model is used. Figure 3 shows the SET–RESET mechanism in TCAD.

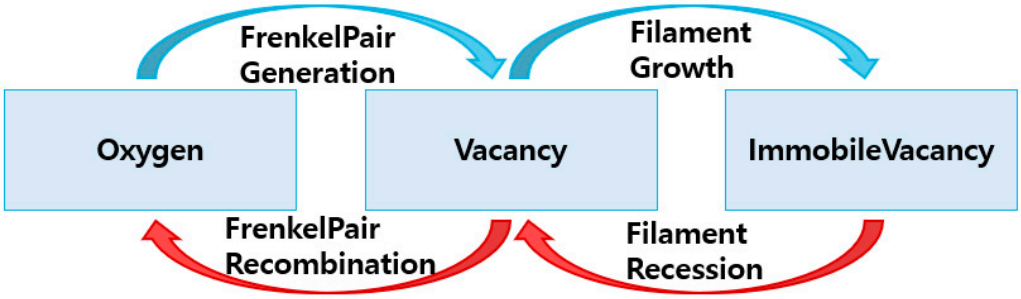

Figure 3. Formation and rupture mechanisms of conductive filaments using the KMC event.

The oxygen ions are defined as *Particle1* in TCAD, representing non-conductive defects. This is applicable to diffusion and generation/recombination events. The oxygen ions and vacancies generate Frenkel defects during diffusion. The vacancies can diffuse within insulator and can be converted back into oxygen ions through recombination events. The vacancies are defined as *Particles2* in TCAD. Additionally, growth/recession events are added to vacancy. When sufficient vacancies diffuse, the conductive defects, known as filaments, are converted through growth events. When a recession event occurs, the filament is transformed back into vacancies. To simulate ReRAM in TCAD, SDevice must satisfy several conditions. First, we define traps, KMC defects, and particle/filament in the global *Physics* syntax. Next, KMC defects are set in the material *Physics* syntax based on the material, and the events are set as shown in Table 1.

Table 1. Physical event support.

Physical Event	Keywords	Relevant Equation
Diffusion	Diffusion	$A(r_1) \rightarrow A(r_2)$
Bulk generation or recombination	Generation, Recombination	$0 \Leftrightarrow A(r) + B(r)$
Interface generation or recombination	Generation, Recombination	$0 \Leftrightarrow A(r_1) + B(r_2)$
Filament growth or recession	Filament growth, Filament recession	$F(r) \Leftrightarrow A(r)$

The event rate is expressed as follows

$$r = v\, exp\left[-\frac{E_A - pF}{k_B T}\right] \quad (1)$$

where v is the maximum rate of events, E_A is the activation energy, p represents a molecular dipole, T is the temperature, k_B is Boltzmann constant, and F denotes an electric field. For generation/recombination events occurring in the bulk, Frenkel pairs should be defined in the same domain, while for an interface, they should be defined in two different domains [42]. The KMC model provides trap-assisted-tunneling (TAT) model and a steady-state heat equation. The two models can be used to obtain realistic ReRAM characteristics. The TAT model utilizes Poole–Frenkel emission, which describes the emission of electrons

from the conduction band of an insulator. The KMC Poole–Frenkel emission rate R_{PF} is given by [42]

$$R_{PF} = v \cdot \exp\left(-\frac{E_D}{k_B T}\right)\left\{\left(\frac{k_B T}{\beta\sqrt{F}}\right)^2\left[1+\left(\frac{\beta\sqrt{F}}{k_B T}-1\right)\exp\left(\frac{\beta\sqrt{F}}{k_B T}\right)\right]+\frac{1}{2}\right\} \quad (2)$$

where F denotes the insulator electric field, v is the lattice vibration frequency, E_D represents the trap depth, ε_{opt} is the insulator optical permittivity and $\beta = \sqrt{\frac{e^3}{\pi\varepsilon_0\varepsilon_{opt}}}$, with the electric charge e and the permittivity of free space ε_o. Table 2 represents the device characterization parameters. These parameters affect the ReRAM event and TAT. The heat equation is represented by [42]

$$\vec{\nabla}\cdot\left(\kappa\vec{\nabla}T + \psi\sigma\vec{\nabla}\psi\right) = 0 \quad (3)$$

where ψ is a potential, κ and σ are electrical and thermal conductivities, which are spatially dependent considering the presence of defects.

Table 2. Device characterization parameters.

	HfO_2	Al_2O_3
Dielectric constant	25 [43]	9 [43]
Optical permittivity	3.74 [44]	3.43 [45]
Band-gap (eV)	5.4 [46]	8.8 [47]
Activation energy (eV)	4.8 [48]	1.8 [48]

4. NeuroSim Simulation

Ideally, the weight increase in long-term potentiation (LTP) and decrease in long-term depression (LTD) should be linearly proportional to the number of input pulses. However, real-world devices are not ideal and typically exhibit a sharp change in conductance in the early stages of LTP and LTD, followed by gradual saturation. NeuroSim uses a model that can capture nonlinear weight-update operations, and the change in conductance with the number of pulses is described by [26]

$$G_{LTP} = B\left(1 - e^{-\frac{P}{A}}\right) + G_{min} \quad (4)$$

$$G_{LTD} = -B\left(1 - e^{\frac{(P-P_{max})}{A}}\right) + G_{max} \quad (5)$$

$$B = (G_{max} - G_{min}) / \left(1 - e^{-\frac{P_{max}}{A}}\right) \quad (6)$$

where P is number of pulses. G_{LTP} and G_{LTD} represent the conductance of LTP and LTD, respectively. G_{max} and G_{min} indicate the maximum and minimum conductance, respectively. P_{max} is defined as the maximum number of pulses required for the device to transition from minimum to maximum conduction. These values are directly extracted from experimental data. A is a variable that controls the nonlinear operation of weight updates. A of LTP and LTD is obtained by fitting in MATLAB R2022a. B is fitted within the ranges the G_{max}, G_{min}, P_{max} and A. Upon completing fitting, the normalized value of A can be verified to identify the nonlinearity label, as shown in Figure 4, which is an example of fitting ReRAM weight updates. The actual conductance varies from cycle to cycle. This variation will be reflected in the weight update, resulting in a rough adjustment. NeuroSim provides nonlinearity label values that correspond to the normalized A values in the Nonlinearity-NormA.htm file. The nonlinearity label A provides a sufficiently precise value at 0–9 in 0.01 increments. If the A is negative, a negative value can be used for the nonlinearity label as well. The A obtained here are used in NeuroSim simulation.

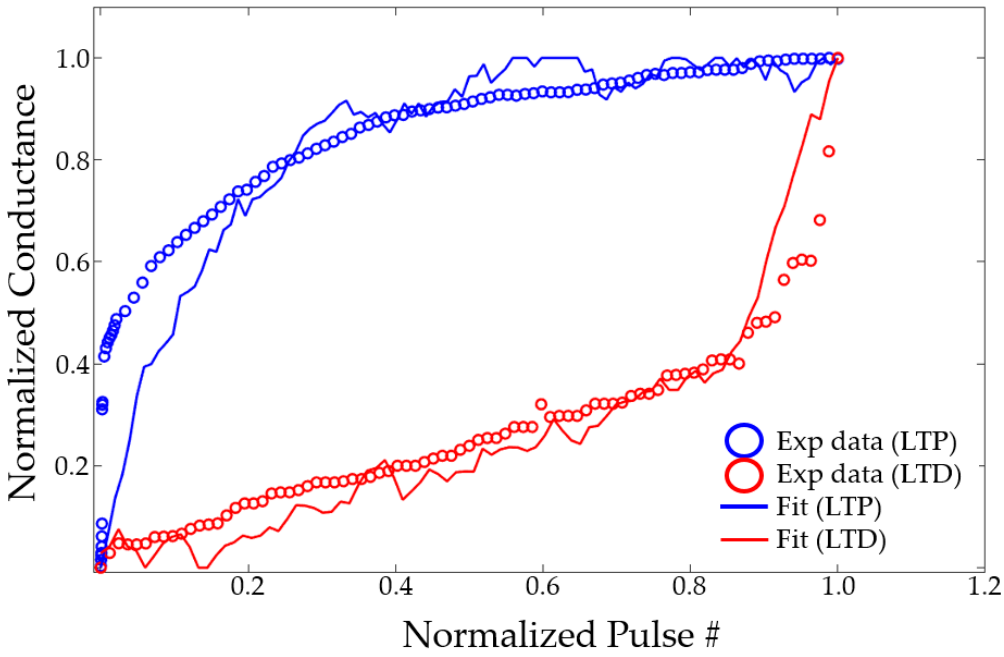

Figure 4. Fitting of ReRAM weight-update data. Normalized conductance and number of pulses is fitted with *A* values.

The conductance of each structure is extracted, and the accuracy of the extracted values is verified with NeuroSim. It is developed to mimic an online/offline learning classification scenario using the MNIST handwriting dataset in a multilayer perceptron (MLP) neural network [26]. As shown in Figure 5, this neural network comprises an input layer, a hidden layer, and an output layer.

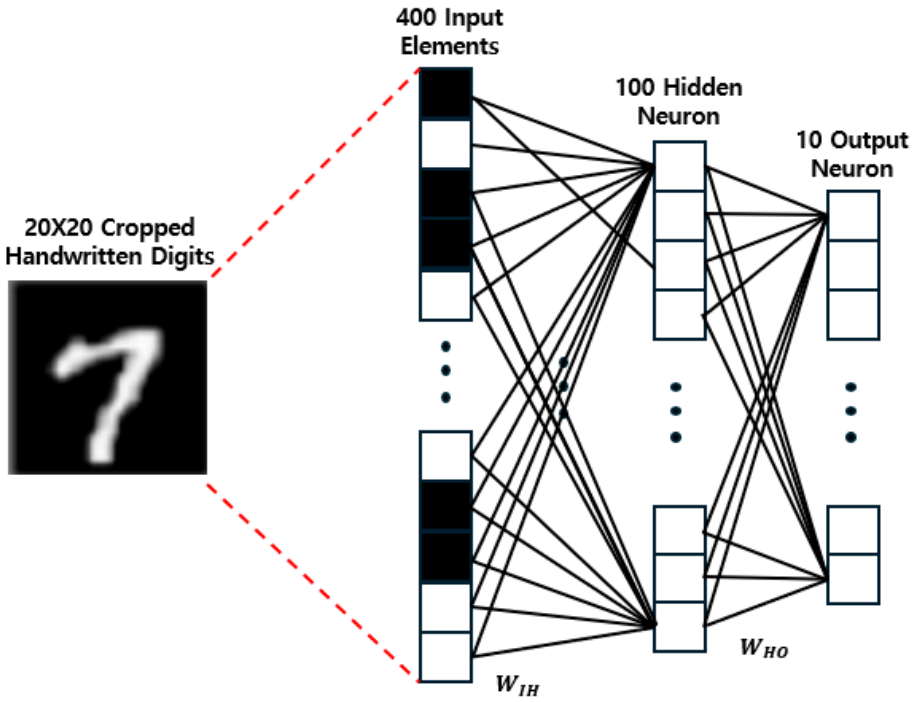

Figure 5. Two-layer MLP neural network for MNIST.

MLP is a fully connected neural network in which every neuron in each layer is connected to every neuron in the next layer. Connections of neurons are made through synapses, and the strength of a synapse represents its weight. W_{IH} and W_{HO} are weight

matrices between the input and hidden layers and hidden and output layers, respectively. The input image data are an MNIST handwritten digit and comprise 20 × 20 pixels. The topology of the network is 400 (input layer)–100 (hidden layer)–10 (output layer). A total of 400 neurons in the input layer corresponds to a 20 × 20 MNIST image, and 10 neurons in the output layer represent 10 classes of numbers. Users can change the network topology as needed.

5. Result and Discussion

The ReRAM device proposed in this study has a Ti layer between the TiN top and bottom electrodes and an active layer comprising one or two insulators. As shown in Figure 6a, the basic structure comprises a 1 nm thick HfO_x and a TiO_x layer inserted between a 10 nm-thick HfO_2 layer and a 5 nm-thick Ti layer. The insertion of HfO_x and TiO_x yields an unstable interface. Using an active electrode material in combination, rather than the single structure of HfO_2, improves its interfacial properties and stabilizes the switching characteristics of ReRAM due to the oxygen adsorption effect [35,36]. Figure 6b shows that the oxide layer is made of 6 nm-thick HfO_2 and 4 nm-thick Al_2O_3 and embodies a multilayer structure. This structure improves the uniformity of the switching voltage and dispersion of HRS resistance [49]. Additionally, inserting a thin layer of Al_2O_3 between the HfO_2 layer and electrode reduces data retention and operating current [50]. Figure 6c depicts a tri-layer structure with a thin layer of Al_2O_3 inserted between the HfO_2 layers. This structure improves the uniformity and stability of switching and allows for the precise control of conductive filaments [38,51].

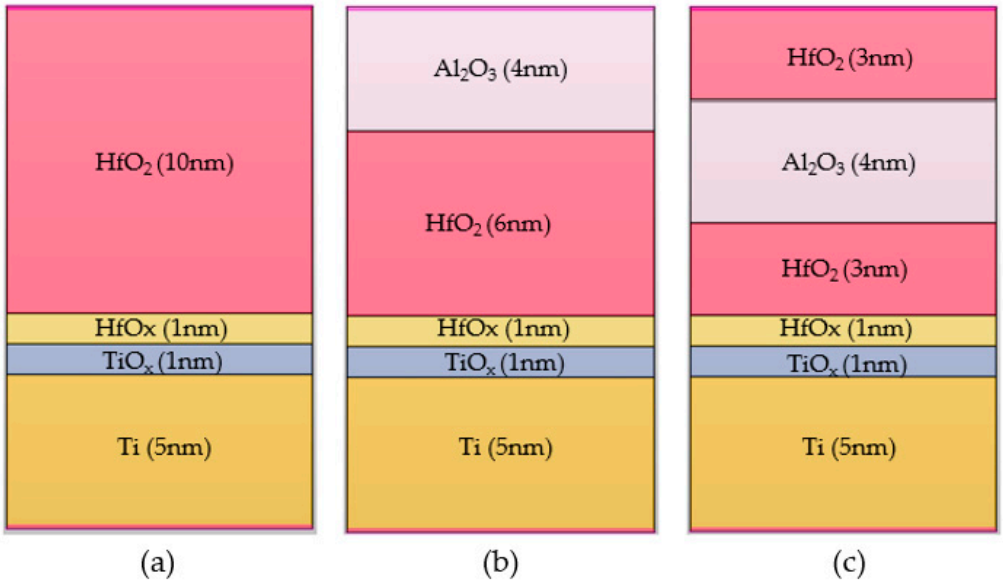

Figure 6. ReRAM structures fabricated with TCAD: (**a**) TiN/Ti/HfO_2/TiN, (**b**) TiN/Ti/HfO_2/Al_2O_3/TiN, and (**c**) TiN/Ti/HfO_2/Al_2O_3/HfO_2/TiN. The top and bottom electrode TiN are not shown in simulation.

The compliance current for ReRAM devices is set at 1 µA. Figure 7 shows the I–V characteristics according to the compliance current. A lower compliance current implies that the reset process starts at a lower voltage because the filament is not sufficiently formed. Additionally, a higher compliance current indicates that the filament is not fully ruptured and does not reform, meaning that the set/reset process does not occur. The voltage is swept from 3V to −3V. The I–V characteristics for the voltage sweep are shown in Figure 8. Early TiN/Ti/HfO_2/TiN devices are formed at 2.85 V. Over several cycles of voltage sweeps, the SET voltage occurs in the range of 2.1 to 2.5 V, and the RESET voltage appears in the range of −1.5 to −2.9 V. HfO_2-Al_2O_3 based device shows improved

uniformity at RESET, while TiN/Ti/HfO_2/TiN exhibits scattered switching characteristics over multiple cycles.

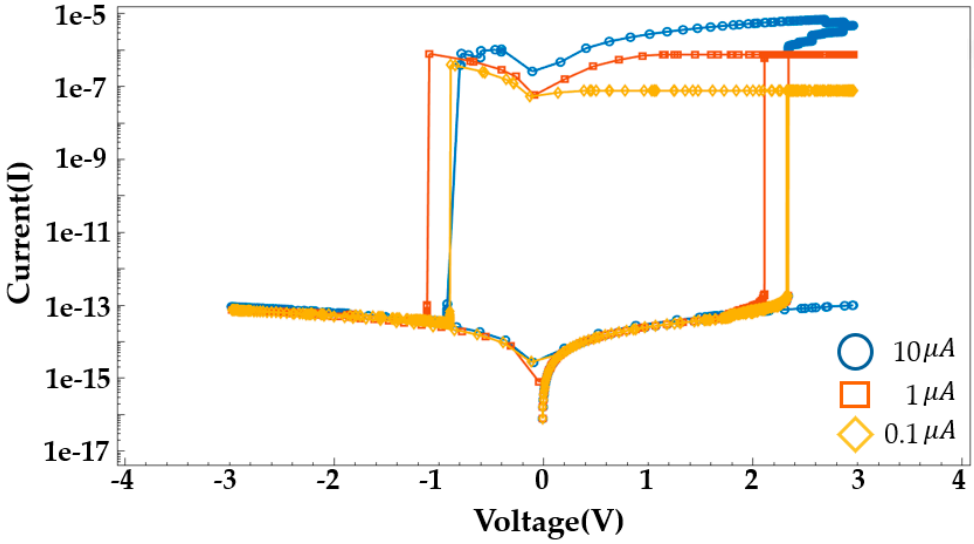

Figure 7. I–V characteristics according to the compliance current.

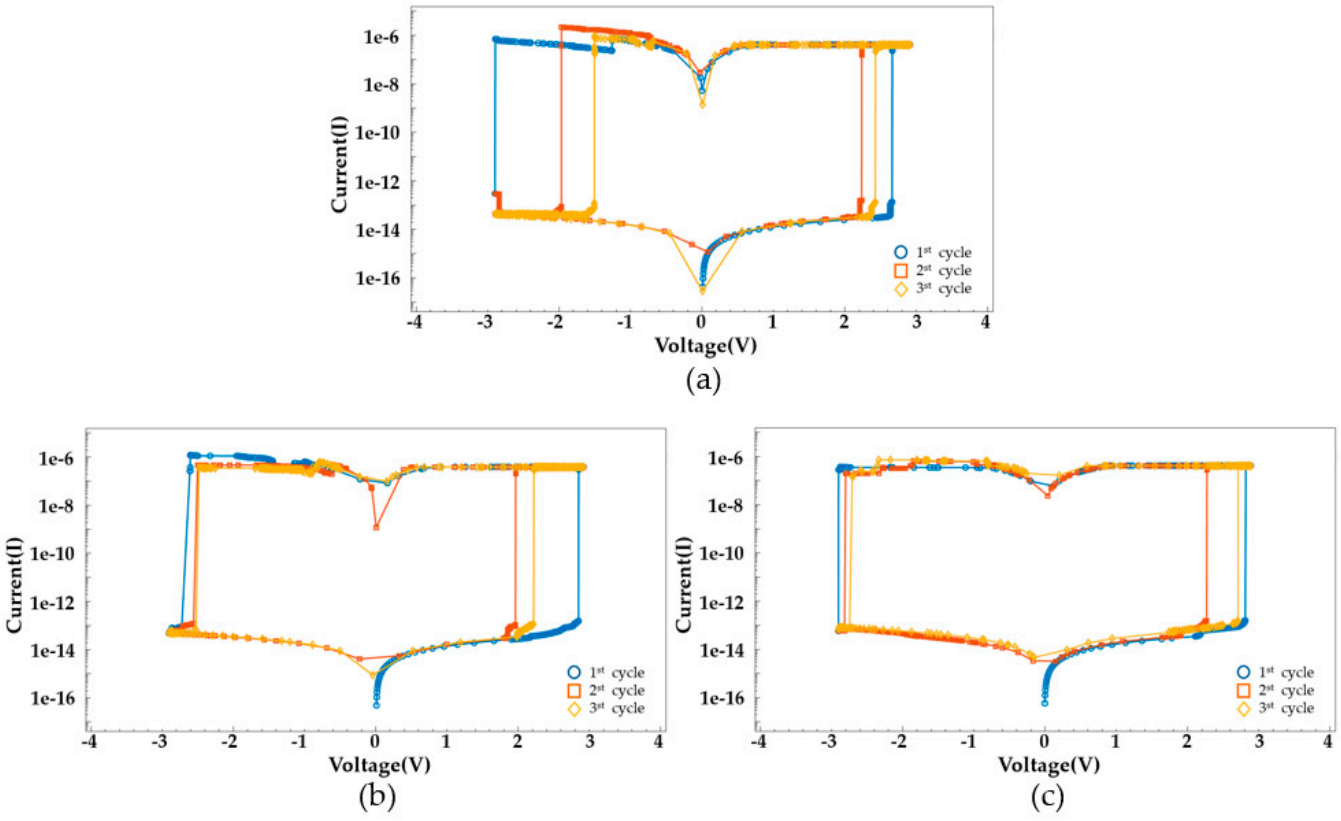

Figure 8. Ideal I–V switching characteristics for different cycles of (**a**) TiN/Ti/HfO_2/TiN, (**b**) TiN/Ti/HfO_2/Al_2O_3/TiN, and (**c**) TiN/Ti/HfO_2/$Al_2O_3HfO_2$/TiN.

The I–V characteristic graph indicates that after the first RESET, the second SET occurs at a lower voltage than the first SET. This result implies the presence of filaments left over from the formation and rupture of conductive filaments. Figure 9 depicts changes in the conductive filament during a voltage sweep.

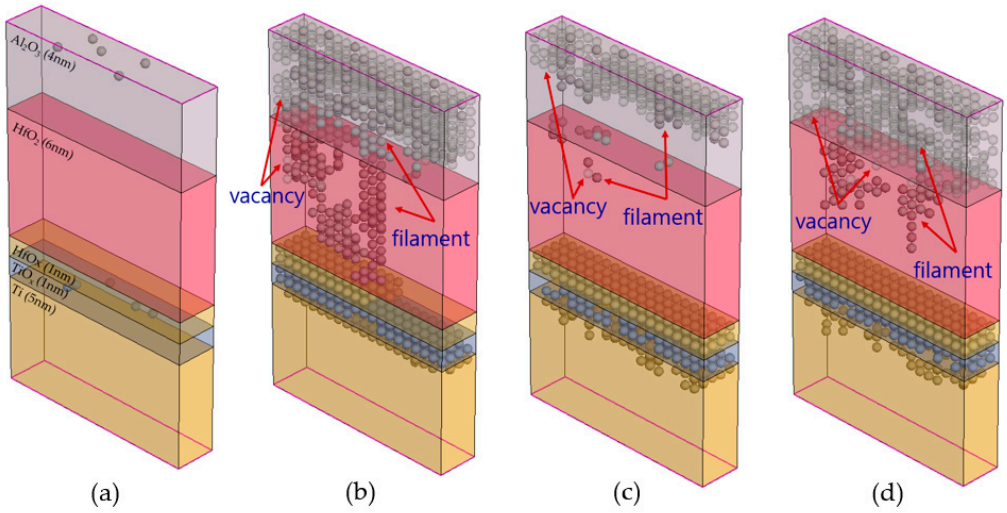

Figure 9. Changes in the conductive filament and oxygen vacancies: (**a**) initial state, (**b**) after the first SET, (**c**) after the first RESET, and (**d**) after the second SET.

Figure 9a shows the initial state with almost no conductive filaments. Figure 9b demonstrates the state after the first SET; here, the input voltage exceeds the threshold value, and a conductive filament is formed to connect the upper and lower electrodes. Figure 9c shows the state after the first RESET, illustrating that a large number of conductive filaments collapsed during the RESET process, while some remained. Figure 9d represents the second SET process, which results in a different shape due to the remnants of conductive filaments. Figure 9 illustrates the migration of oxygen vacancies and filaments. Figure 10 demonstrates the change in conductance for an input pulse with an amplitude of 2.5 V and a period of 2 ms in TCAD.

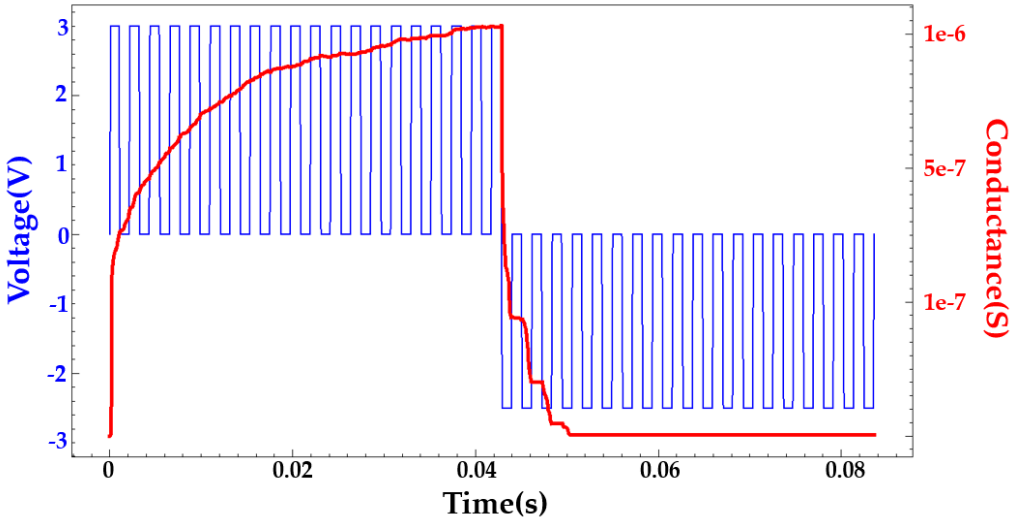

Figure 10. The change in conductance over the identical pulse in TCAD. The positive and negative voltages are 3 V and −2.5 V, respectively.

Figure 11a shows changes in conductance for the same input pulse. Figure 11a(i–iii) demonstrate the conductance change for the TiN/Ti/HfO_2/TiN structure, the conductance change for the TiN/Ti/HfO_2/TiN structure, and the TiN/Ti/HfO_2/Al_2O_3/HfO_2/TiN structure, respectively. In Figure 11a, the multi-level states of conductance are shown by averaging the conductance from cycle to cycle. In addition, the coordination of pulses can create multi-level states. When the same pulse is employed, the TiN/Ti/HfO_2/TiN structure shows a gradual increase and a sharp change in conductance. The TiN/Ti/HfO_2/Al_2O_3/TiN structure exhibits a sharp increase and a gradual decrease, while the TiN/Ti/HfO_2/Al_2O_3/

HfO_2/TiN structure demonstrates a gradual increase and decrease. The SET–RESET voltage obtained from TCAD simulation, change in conductance over time, and normalized *A* values yielded from the MATLAB fitting are applied to NeuroSim simulation. The conductance of each structure is averaged over 30 random cycles. The deviations of cycle-to-cycle are reflected in the NeuroSim simulation.

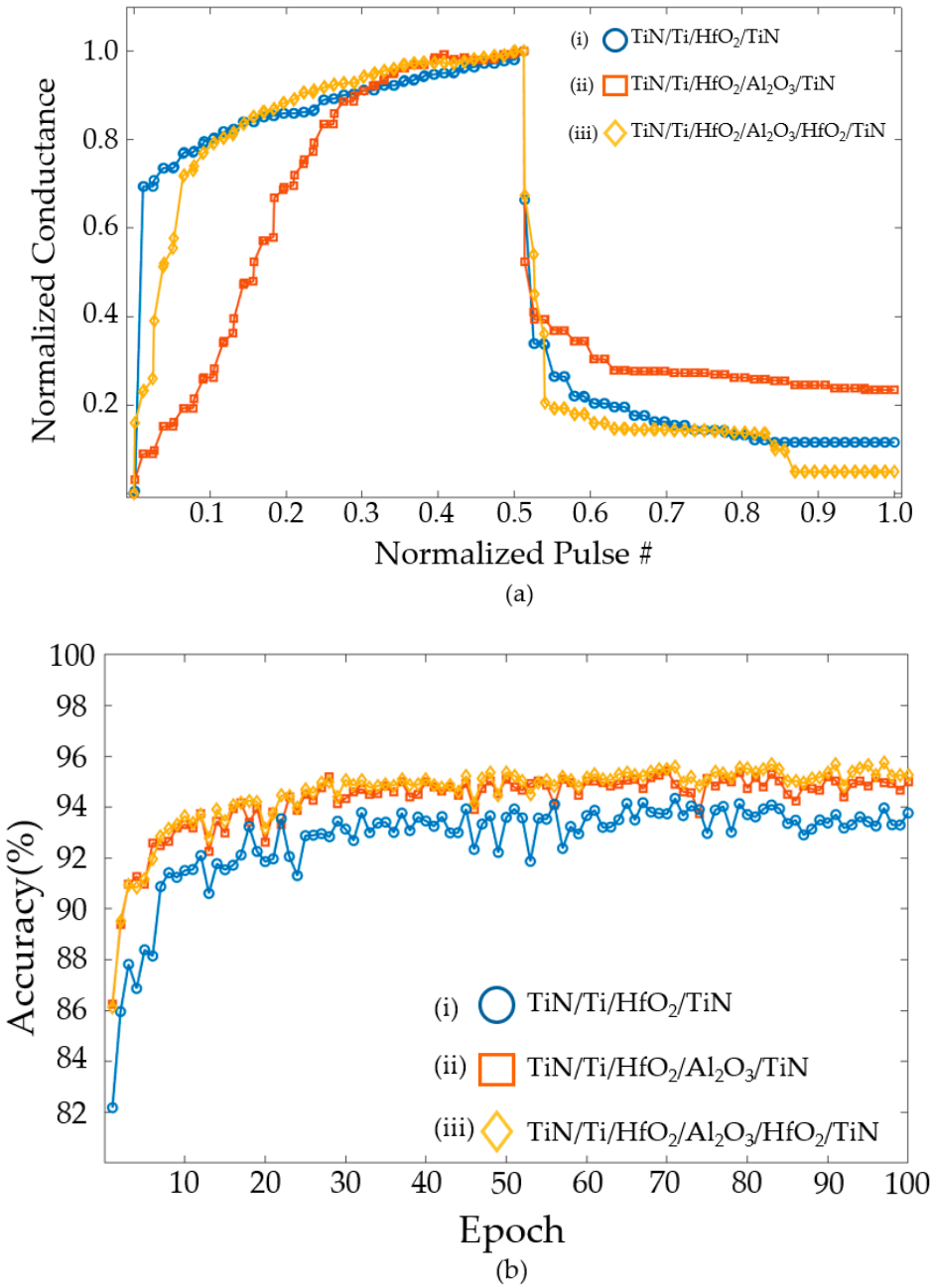

Figure 11. (**a**) Conductance changes and (**b**) accuracy for (**i**) TiN/Ti/HfO_2/TiN, (**ii**) TiN/Ti/HfO_2/Al_2O_3/TiN, and (**iii**) TiN/Ti/HfO_2/Al_2O_3/HfO_2/TiN structures.

A neural network trained using randomly selected images from a training dataset (60,000 images) and a test dataset (10,000 images) is classified. Figure 11b shows the results of a simulation with Epoch set to 100. Each device is verified for accuracy using NeuroSim. The TiN/Ti/HfO_2/TiN structure yields an average accuracy of 92.73% and the highest accuracy of 94.35%. The TiN/Ti/HfO_2/Al_2O_3/TiN structure exhibits an average accuracy of 94.27% and the highest accuracy of 95.43%. The TiN/Ti/HfO_2/Al_2O_3/HfO_2/TiN structure demonstrates an average accuracy of 94.56 and the highest accuracy of 95.76%.

Figure 12 illustrates the I–V switching characteristics with a tunneling process. During a SET event, the current behavior is more nonlinear than the I–V characteristic in Figure 8, resulting in the change in conductance. The high temperature causes non-uniformity and diffusion in filament growth and also promotes the TAT process. Therefore, it should be included to obtain realistic I–V characteristics. Figure 13 shows an example of the temperature-dependent I–V characteristics in the HfO_2/Al_2O_3 structure. SET and RESET occur at lower voltages as temperature increases because the filament formation and rupture become more active at higher temperatures. Additionally, tunneling effects are more pronounced at elevated temperatures.

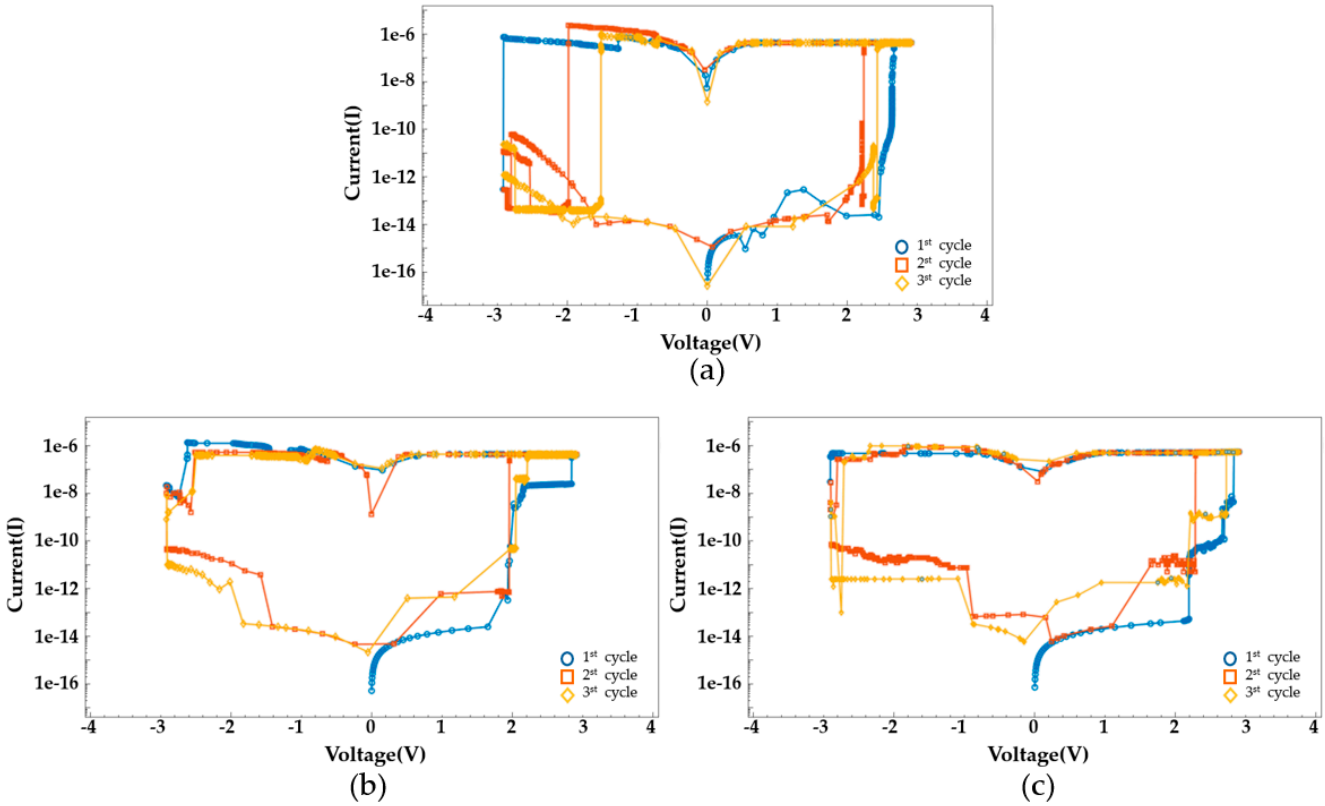

Figure 12. I–V switching characteristics with TAT for different cycles of (**a**) TiN/Ti/HfO_2/TiN, (**b**) TiN/Ti/HfO_2/Al_2O_3/TiN, and (**c**) TiN/Ti/HfO_2/$Al_2O_3$$HfO_2$/TiN.

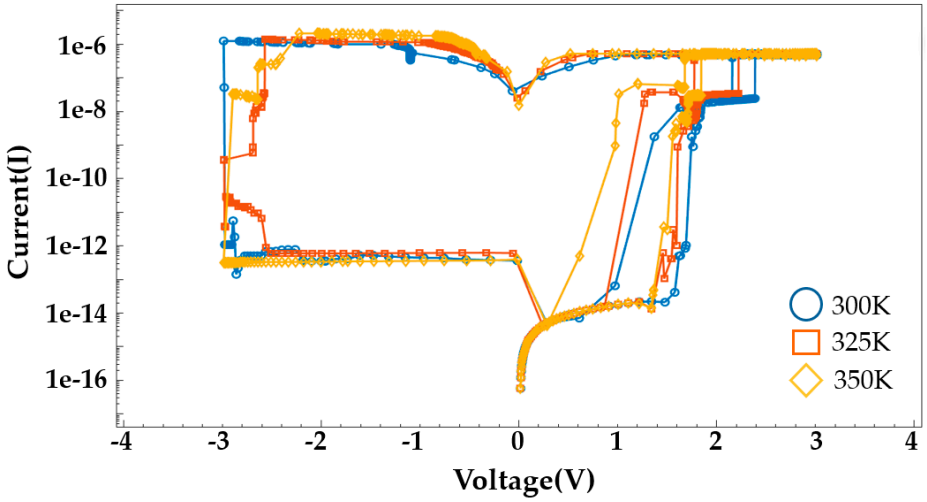

Figure 13. The temperature-dependent I–V characteristics in the HfO_2/Al_2O_3 structure.

Figure 14a displays the change in conductivity in a simulation with tunneling. The conductance sharply increases in the potentiation and gradually decreases in a depression. Each conductance is the average of the data over 30 cycles. The accuracy verification of these results is shown in Figure 14b. The TiN/Ti/HfO_2/TiN structure yields an average accuracy of 84.47% and the highest accuracy of 87.71%. The TiN/Ti/HfO_2/Al_2O_3/TiN structure exhibits an average accuracy of 86.03% and the highest accuracy of 89.73%. The TiN/Ti/HfO_2/Al_2O_3/HfO_2/TiN structure demonstrates an average accuracy of 87.99% and the highest accuracy of 90.37%. This represents a decrease of approximately 4–7%, compared to the accuracy shown in Figure 11b. This is due to the fact that the conductance changes due to tunneling are more asymmetric than the ideal case.

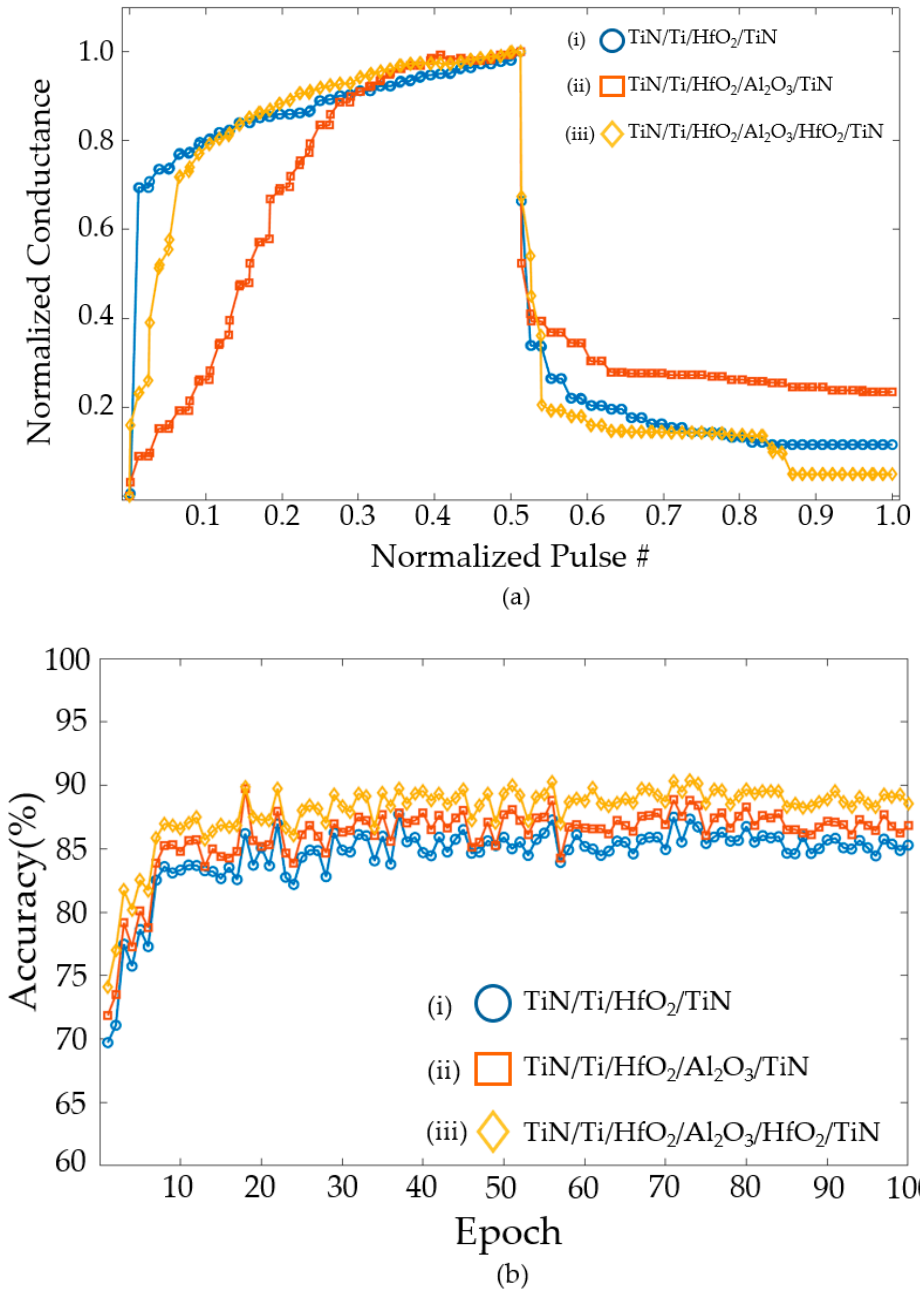

Figure 14. (**a**) Conductance change and (**b**) accuracy for (**i**) TiN/Ti/HfO_2/TiN, (**ii**) TiN/Ti/HfO_2/Al_2O_3/TiN, and (**iii**) TiN/Ti/HfO_2/Al_2O_3/HfO_2/TiN structures with TAT.

Inconsistent conductance changes make it difficult to reach the target conductance with the same pulse, reducing the convergence rate during the learning process. Nonlinear-

ity and asymmetry affect learning accuracy. Nonlinearity causes more training accuracy loss. However, the bidirectional symmetric incremental conductance change has been found to maintain good accuracy even with relatively high nonlinearity. As the number of cycles increases, endurance gradually decreases. Additionally, with more cycles, functional reliability metrics such as dynamic range, nonlinearity, and asymmetry gradually deteriorate, leading to reduced accuracy [52].

6. Conclusions

In this paper, we presented the characterization of HfO_2-based ReRAMs using Sentaurus TCAD. The switching behavior of the ReRAM is implemented through the KMC model, accounting for the application of the TAT model to describe the real device. The TCAD simulation performs the insertion of Al_2O_3 in the device, which is shown to display improved switching behavior. The device characteristics extracted from TCAD are used to evaluate the impact of ReRAM configuration on neuromorphic computing in NeuroSim. An idealized ReRAM would have high accuracy in a neuromorphic computing system. However, simulations with added tunneling show relatively low accuracy, implying that the accuracy of the conductance change depends on the asymmetric shape. As a result, TCAD can flexibly simulate various structures and processes, and characterize the properties of real devices. In support of TCAD simulation, an efficient verification of various ReRAM devices for neuromorphic computing can be achieved, enabling the acceleration ofthe pace of research by quickly finding ways to optimize device design.

Author Contributions: Conceptualization, S.K. and J.L.; methodology, J.L.; software, S.K.; validation, S.K. and J.L.; writing—original draft preparation, S.K.; writing—review and editing, S.K. and J.L.; visualization, S.K.; supervision, J.L.; project administration, J.L.; funding acquisition, J.L. All authors have read and agreed to the published version of the manuscript.

Funding: This work is funded by a 2024 research Grant from Sangmyung University.

Data Availability Statement: The data present in this study are available on request from the corresponding author.

Conflicts of Interest: The authors declare no conflicts of interest.

References

1. Silver, D.; Huang, A.; Maddison, C.J.; Guez, A.; Sifre, L.; van den Driessche, G.; Schrittwieser, J.; Antonoglou, I.; Panneershelvam, V.; Lanctot, M.; et al. Mastering the game of Go with deep neural networks and tree search. *Nature* **2016**, *529*, 484–489. [CrossRef]
2. Graves, A.; Wayne, G.; Reynolds, M.; Harley, T.; Danihelka, I.; Grabska-Barwińska, A.; Colmenarejo, S.G.; Grefenstette, E.; Ramalho, T.; Agapiou, J.; et al. Hybrid computing using a neural network with dynamic external memory. *Nature* **2016**, *538*, 471–476. [CrossRef]
3. Ielmini, D.; Wong, H.-S.P. In-memory computing with resistive switching devices. *Nat. Electron.* **2018**, *1*, 333–343. [CrossRef]
4. Merces, L.; Ferro, L.M.M.; Thomas, A.; Karnaushenko, D.D.; Luo, Y.; Egunov, A.I.; Zhang, W.; Bandari, V.K.; Lee, Y.; McCaskill, J.S.; et al. Bio-inspired dynamically morphing microelectronics toward high-density energy applications and intelligent biomedical Implants. *Adv. Mater.* **2024**, *36*, e2313327. [CrossRef] [PubMed]
5. Wang, S.; Chen, X.; Zhao, C.; Kong, Y.; Lin, B.; Wu, Y.; Bi, Z.; Xuan, Z.; Li, T.; Li, Y.; et al. An organic electrochemical transistor for multi-modal sensing, memory and processing. *Nat. Electron.* **2023**, *6*, 281–291. [CrossRef]
6. Najafabadi, M.M.; Villanustre, F.; Khoshgoftaar, T.M.; Seliya, N.; Wald, R.; Muharemagic, E. Deep learning applications and challenges in big data analytics. *J. Big Data* **2015**, *2*, 1. [CrossRef]
7. Peteiro-Barral, D.; Guijarro-Berdiñas, B. A survey of methods for distributed machine learning. *Prog. Artif. Intell.* **2012**, *2*, 1–11. [CrossRef]
8. Maass, W.; Markram, H. On the computational power of circuits of spiking neurons. *J. Comput. Syst. Sci.* **2004**, *69*, 593–616. [CrossRef]
9. Gambuzza, L.V.; Frasca, M.; Fortuna, L.; Ntinas, V.; Vourkas, I.; Sirakoulis, G.C. Memristor crossbar for adaptive synchronization. *IEEE Trans. Circuits Syst. I Regul. Pap.* **2017**, *64*, 2124–2133. [CrossRef]
10. Ding, G.; Li, H.; Zhao, J.; Zhou, K.; Zhai, Y.; Lv, Z.; Zhang, M.; Yan, Y.; Han, S.-T.; Zhou, Y. Nanomaterials for flexible neuromorphics. *Chem. Rev.* **2024**. [CrossRef]
11. Merces, L.; Ferro, L.M.M.; Nawaz, A.; Sonar, P. Advanced neuromorphic applications enabled by synaptic ion-gating vertical transistors. *Adv. Sci.* **2024**, *11*, e2305611. [CrossRef] [PubMed]

12. Zhang, X.; Huang, A.; Hu, Q.; Xiao, Z.; Chu, P.K. Neuromorphic computing with memristor crossbar. *Phys. Status Solidi (A)* **2018**, *215*, 1700875. [CrossRef]
13. Choi, B.J.; Torrezan, A.C.; Strachan, J.P.; Kotula, P.G.; Lohn, A.J.; Marinella, M.J.; Li, Z.; Williams, R.S.; Yang, J.J. High-speed and low-energy nitride memristors. *Adv. Funct. Mater.* **2016**, *26*, 5290–5296. [CrossRef]
14. Chua, L. Memristor-the missing circuit element. *IEEE Trans. Circuit Theory* **1971**, *18*, 507–519. [CrossRef]
15. Wang, H.; Yan, X. Overview of resistive random access memory (RRAM): Materials, filament mechanisms, performance optimization, and prospects. *Phys. Status Solidi (RRL)* **2019**, *13*, 1900073. [CrossRef]
16. Younis, A.; Li, S. Microscopic investigations of switching phenomenon in memristive systems: A mini review. *RSC Adv.* **2018**, *8*, 28763–28774. [CrossRef]
17. Dong, X.; Jouppi, N.P.; Xie, Y. PCRAMsim: System-level performance, energy, and area modeling for phase-change RAM. In Proceedings of the 2009 International Conference on Computer-Aided Design, San Jose, CA, USA, 26–29 November 2009; pp. 269–275. [CrossRef]
18. Li, Y.; Wang, Z.; Midya, R.; Xia, Q.; Yang, J.J. Review of memristor devices in neuromorphic computing: Materials sciences and device challenges. *J. Phys. D Appl. Phys.* **2018**, *51*, 503002. [CrossRef]
19. Yang, Y.; Lu, W. Nanoscale resistive switching devices: Mechanisms and modeling. *Nanoscale* **2013**, *5*, 10076. [CrossRef]
20. Ishiwara, H. FeFET and ferroelectric random access memories. In *Multifunctional Oxide Heterostructures*; Oxford University Press: Oxford, UK, 2012; pp. 340–363. [CrossRef]
21. Garbin, D.; Vianello, E.; Bichler, O.; Rafhay, Q.; Gamrat, C.; Ghibaudo, G.; DeSalvo, B.; Perniola, L. HfO_2-based O_xRAM devices as synapses for convolutional neural networks. *IEEE Trans. Electron Devices* **2015**, *62*, 2494–2501. [CrossRef]
22. Gao, B.; Bi, Y.; Chen, H.-Y.; Liu, R.; Huang, P.; Chen, B.; Liu, L.; Liu, X.; Yu, S.; Wong, H.-S.P.; et al. Ultra-low-energy three-dimensional oxide-based electronic synapses for implementation of robust high-accuracy neuromorphic computation systems. *ACS Nano* **2014**, *8*, 6998–7004. [CrossRef]
23. Liu, G.; Li, Q.; Shi, W.; Liu, Y.; Liu, K.; Yang, X.; Shao, M.; Guo, A.; Huang, X.; Zhang, F.; et al. Ultralow-power and multisensory artificial synapse based on electrolyte-gated vertical organic transistors. *Adv. Funct. Mater.* **2022**, *32*, 2200959. [CrossRef]
24. Hong, X.; Loy, D.J.; Dananjaya, P.A.; Tan, F.; Ng, C.; Lew, W. Oxide-based RRAM materials for neuromorphic computing. *J. Mater. Sci.* **2018**, *53*, 8720–8746. [CrossRef]
25. Vianello, E.; Thomas, O.; Molas, G.; Turkyilmaz, O.; Jovanovic, N.; Garbin, D.; Palma, G.; Alayan, M.; Nguyen, C.; Coignus, J.; et al. Resistive memories for ultra-low-power embedded computing design. In Proceedings of the 2014 IEEE International Electron Devices Meeting, San Francisco, CA, USA, 15–17 December 2014; Volume 40, pp. 1–6. [CrossRef]
26. Chen, P.-Y.; Peng, X.; Yu, S. NeuroSim+: An integrated device-to-algorithm framework for benchmarking synaptic devices and array architectures. In Proceedings of the 2017 IEEE International Electron Devices Meeting (IEDM), San Francisco, CA, USA, 2–6 December 2017. [CrossRef]
27. Brivio, S.; Tallarida, G.; Cianci, E.; Spiga, S. Formation and disruption of conductive filaments in a HfO_2/TiN structure. *Nanotechnology* **2014**, *25*, 385705. [CrossRef] [PubMed]
28. Lanza, M. A review on resistive switching in high-k dielectrics: A nanoscale point of view using conductive atomic force microscope. *Materials* **2014**, *7*, 2155–2182. [CrossRef]
29. Ielmini, D. Modeling the universal set/reset characteristics of bipolar RRAM by field- and temperature-driven filament growth. *IEEE Trans. Electron Devices* **2011**, *58*, 4309–4317. [CrossRef]
30. Brivio, S.; Frascaroli, J.; Spiga, S. Role of metal-oxide interfaces in the multiple resistance switching regimes of Pt/HfO_2/TiN devices. *Appl. Phys. Lett.* **2015**, *107*, 023504. [CrossRef]
31. Yu, S.; Wong, H.-S.P. A phenomenological model for the reset mechanism of metal oxide RRAM. *IEEE Electron Device Lett.* **2010**, *31*, 1455–1457. [CrossRef]
32. Jiang, R.; Han, Z.; Du, X. Reliability/uniformity improvement induced by an ultrathin TiO_2 insertion in Ti/HfO_2/Pt resistive switching memories. *Microelectron. Reliab.* **2016**, *63*, 37–41. [CrossRef]
33. Nakajima, R.; Azuma, A.; Yoshida, H.; Shimizu, T.; Ito, T.; Shingubara, S. Hf layer thickness dependence of resistive switching characteristics of Ti/Hf/HfO_2/Au resistive random access memory device. *Jpn. J. Appl. Phys.* **2018**, *57*, 06HD06. [CrossRef]
34. Tsunoda, K.; Kinoshita, K.; Noshiro, H.; Yamazaki, Y.; Iizuka, T.; Ito, Y.; Takahashi, A.; Okano, A.; Sato, Y.; Fukano, T.; et al. Low power and high speed switching of Ti-doped NiO ReRAM under the unipolar voltage source of less than 3 V. In Proceedings of the 2007 IEEE International Electron Devices Meeting, Washington, DC, USA, 10–12 December 2007; pp. 767–770. [CrossRef]
35. Chen, Y.Y.; Pourtois, G.; Clima, S.; Govoreanu, B.; Goux, L.; Fantini, A.; Degreave, R.; Groeseneken, G.; Wouters, D.; Jurczak, M. Hf Cap Thickness Dependence in Bipolar-Switching TiN\HfO_2\Hf\TiN RRAM Device. *ECS Trans.* **2012**, *50*, 3. [CrossRef]
36. De Stefano, F.; Houssa, M.; Afanas'ev, V.V.; Kittl, J.A.; Jurczak, M.; Stesmans, A. Nature of the filament formed in HfO_2-based resistive random access memory. *Thin Solid Films* **2013**, *533*, 15–18. [CrossRef]
37. Zhang, W.; Kong, J.-Z.; Cao, Z.-Y.; Li, A.-D.; Wang, L.-G.; Zhu, L.; Li, X.; Cao, Y.-Q.; Wu, D. Bipolar resistive switching characteristics of HfO_2/TiO_2/HfO_2 trilayer-structure RRAM devices on Pt and TiN-coated substrates fabricated by atomic layer deposition. *Nanoscale Res. Lett.* **2017**, *12*, 393. [CrossRef] [PubMed]
38. Vinuesa, G.; Ossorio, O.; García, H.; Sahelices, B.; Castán, H.; Dueñas, S.; Kull, M.; Tarre, A.; Jogiaas, T.; Tamm, A.; et al. Effective control of filament efficiency by means of spacer $HfAlO_x$ layers and growth temperature in HfO_2 based ReRAM devices. *Solid-State Electron.* **2021**, *183*, 108085. [CrossRef]

39. Alayan, M.; Vianello, E.; Larcher, L.; Padovani, A.; Levisse, A.; Castellani, N.; Charpin, C.; Bernasconi, S.; Molas, G.; Portal, J.-M.; et al. Self-rectifying behavior and analog switching under identical pulses using tri-layer RRAM crossbar array for neuromorphic systems. In Proceedings of the 2017 IEEE International Memory Workshop (IMW), Monterey, CA, USA, 14–17 May 2017; pp. 1–4. [CrossRef]
40. Guan, X.; Yu, S.; Wong, H.-S.P. On the switching parameter variation of metal-oxide RRAM—Part I: Physical modeling and simulation methodology. *IEEE Trans. Electron Devices* **2012**, *59*, 1172–1182. [CrossRef]
41. Russo, U.; Ielmini, D.; Cagli, C.; Lacaita, A.L. Self-accelerated thermal dissolution model for reset programming in unipolar resistive-switching memory (RRAM) devices. *IEEE Trans. Electron Devices* **2009**, *56*, 193–200. [CrossRef]
42. Synopsys. Available online: https://solvnet.synopsys.com (accessed on 15 August 2024).
43. Azadmanjiri, J.; Berndt, C.C.; Wang, J.; Kapoor, A.; Srivastava, V.K.; Wen, C. A review on hybrid nanolaminate materials synthesized by deposition techniques for energy storage applications. *J. Mater. Chem. A* **2014**, *2*, 3695–3708. [CrossRef]
44. Dominguez, O.; McGinnity, T.L.; Roeder, R.K.; Hoffman, A.J. Optical characterization of polar HfO_2 nanoparticles in the mid- and far-infrared. *Appl. Phys. Lett.* **2017**, *111*, 011101. [CrossRef]
45. Taha, T.A. Optical properties of PVC/Al_2O_3 nanocomposite films. *Polym. Bull.* **2018**, *76*, 903–918. [CrossRef]
46. Fadida, S.; Eizenberg, M.; Nyns, L.; Van Elshocht, S.; Caymax, M. Band alignment of Hf–Zr oxides on Al_2O_3/GeO_2/Ge stacks. *Microelectron. Eng.* **2011**, *88*, 1557–1559. [CrossRef]
47. Filatova, E.O.; Konashuk, A.S. Interpretation of the changing the band gap of Al_2O_3 depending on its crystalline form: Connection with different local symmetries. *J. Phys. Chem. C* **2015**, *119*, 20755–20761. [CrossRef]
48. Sarkar, B.; Lee, B.; Misra, V. Implications of lower zero-field activation energy of dielectric in Al_2O_3/HfO_2 bi-layer dielectric RRAM Forming Process. *ECS Trans.* **2014**, *64*, 43–48. [CrossRef]
49. Yu, S.; Wu, Y.; Chai, Y.; Provine, J.; Wong, H.-S.P. Characterization of switching parameters and multilevel capability in HfO_x/AlO_x Bi-layer RRAM devices. In Proceedings of the 2011 International Symposium on VLSI Technology, Systems and Applications, Hsinchu, Taiwan, 25–27 April 2011; pp. 1–2. [CrossRef]
50. Kim, W. Effect of inserting Al_2O_3 layer and device structure in HfO_2-based ReRAM for low power operation. In Proceedings of the 2012 4th IEEE International Memory Workshop, Milan, Italy, 20–23 May 2012; pp. 1–4. [CrossRef]
51. Mahata, C.; Kang, M.; Kim, S. Multi-level analog resistive switching characteristics in tri-Layer HfO_2/Al_2O_3/HfO_2 based memristor on ITO electrode. *Nanomaterials* **2020**, *10*, 2069. [CrossRef] [PubMed]
52. Zhao, M.; Gao, B.; Tang, J.; Qian, H.; Wu, H. Reliability of analog resistive switching memory for neuromorphic computing. *Appl. Phys. Rev.* **2020**, *7*, 011301. [CrossRef]